Protein misfolding occurs by slow diffusion across multiple barriers in a rough energy landscape

Hao Yu[a,1], Derek R. Dee[a,1], Xia Liu[a], Angela M. Brigley[b], Iveta Sosova[b], and Michael T. Woodside[a,b,2]

[a]Department of Physics, University of Alberta, Edmonton, AB, T6G 2E1, Canada; and [b]National Institute for Nanotechnology, National Research Council, Edmonton, AB, T6G 2M9, Canada

Edited by José N. Onuchic, Rice University, Houston, TX, and approved June 1, 2015 (received for review October 5, 2014)

The timescale for the microscopic dynamics of proteins during conformational transitions is set by the intrachain diffusion coefficient, *D*. Despite the central role of protein misfolding and aggregation in many diseases, it has proven challenging to measure *D* for these processes because of their heterogeneity. We used single-molecule force spectroscopy to overcome these challenges and determine *D* for misfolding of the prion protein PrP. Observing directly the misfolding of individual dimers into minimal aggregates, we reconstructed the energy landscape governing nonnative structure formation. Remarkably, rather than displaying multiple pathways, as typically expected for aggregation, PrP dimers were funneled into a thermodynamically stable misfolded state along a single pathway containing several intermediates, one of which blocked native folding. Using Kramers' rate theory, *D* was found to be 1,000-fold slower for misfolding than for native folding, reflecting local roughening of the misfolding landscape, likely due to increased internal friction. The slow diffusion also led to much longer transit times for barrier crossing, allowing transition paths to be observed directly for the first time to our knowledge. These results open a new window onto the microscopic mechanisms governing protein misfolding.

intrachain diffusion | protein aggregation | prion protein | optical tweezers | single-molecule force spectroscopy

The formation of intricate 3D structures by proteins is a complex physical process. Such "folding" is typically described in terms of energy landscape theory (1) as a thermally driven diffusive search over an energy landscape in conformational space for the minimum-energy structure. In this picture, whereas the rates at which structural transitions take place are dominated by the presence of energy barriers in the landscape (2), it is the coefficient of diffusion over the landscape, *D*, that encapsulates the microscopic dynamics of the protein chain, setting the characteristic timescale for molecular motions. Knowledge of *D* provides insight into the internal friction in the protein chain as it undergoes conformational fluctuations (3) and sets the ultimate speed limit at which changes in structure can take place (4).

Given the fundamental importance of the diffusion coefficient in protein folding, there has been much interest in measuring *D* under different conditions. Conformational diffusion has been studied extensively in peptides and unfolded proteins (5–10), using fluorescence probes such as fluorophore quenching or Förster resonant energy transfer to measure reconfiguration times. Typically, $D \sim 10^7$–10^8 nm^2/s was found, although values as low as 10^5 nm^2/s have been reported (10). Because the diffusion coefficient is inversely proportional to friction, measurements of *D* have been important for investigating the role and origin of internal friction along the folding pathway (6, 9). Possible links between the value of *D* and aggregation propensity have also been explored in intrinsically disordered proteins (5). However, it has proven challenging to measure the diffusion coefficient during barrier crossing via fluorescence, owing to the very brief transition time for barrier crossing (11).

Recently, an alternate approach using single-molecule force spectroscopy (SMFS), whereby force is applied to induce structural changes in an isolated molecule, has been applied to measure *D* for barrier crossings (12–15). This approach takes advantage of the powerful ability of force spectroscopy to measure energy landscapes by analyzing the statistics of conformational fluctuations (16), using the landscape profile and rates to recover *D* from Kramers' theory (17). The ability to probe barrier crossings opens up the exciting possibility of investigating the microscopic differences between native structure formation and what happens when folding goes awry, producing nonnative structures. Such misfolding is a feature of many diseases, with misfolded proteins characteristically aggregating into insoluble amyloid fibers rich in β-sheets (18). The value of *D* should be particularly important in misfolding, because the outcome of misfolding and aggregation processes is thought in many cases to be dominated by kinetics (19). Although in silico studies have begun to probe the energy landscapes for protein misfolding and aggregation (20), these landscapes have not yet been reconstructed experimentally. A direct comparison between diffusion in native folding and misfolding of the same protein has therefore not yet been made.

An important challenge in studying misfolding and aggregation is that they are typically very heterogeneous processes, involving various transient species along multiple pathways leading to different types of aggregates (21). Despite recent advances including solving the structures of some native-like aggregation precursor states (22, 23) and small oligomers (24), a full picture of the sequence of molecular events in aggregation remains elusive. Single-molecule assays are well suited to overcome this challenge, through their ability to distinguish and characterize even transient subpopulations with high sensitivity (25). Previous studies have investigated phenomena ranging from transient, metastable misfolding events (26–28) to various stages in the growth of aggregates (29, 30), but complete misfolding pathways leading to stable misfolded states have not yet been elucidated (25).

Significance

Structural transitions in proteins are characterized by the coefficient for intrachain diffusion, *D*, which determines the transition kinetics and reveals microscopic properties of the interactions governing folding. *D* has been measured for unfolded proteins and for native folding, but never for misfolding and aggregation, despite the importance of kinetics for driving these processes. We used single-molecule force spectroscopy to observe the misfolding of individual prion protein (PrP) molecules into stable, nonnative dimers. By reconstructing the energy landscape for dimer misfolding, we compared *D* for misfolding of PrP to that for native folding. Diffusion was 1,000-fold slower for misfolding, reflecting significant additional roughness in the energy landscape and confirming quantitatively the long-held hypothesis that misfolding landscapes are rougher than native landscapes.

Author contributions: M.T.W. designed research; H.Y., D.R.D., and X.L. performed research; A.M.B. and I.S. contributed new reagents/analytic tools; H.Y., D.R.D., and M.T.W. analyzed data; and H.Y., D.R.D., X.L., A.M.B., I.S., and M.T.W. wrote the paper.

The authors declare no conflict of interest.

This article is a PNAS Direct Submission.

[1]H.Y. and D.R.D. contributed equally to this work.

[2]To whom correspondence should be addressed. Email: Michael.Woodside@ualberta.ca.

This article contains supporting information online at www.pnas.org/lookup/suppl/doi:10.1073/pnas.1419197112/-/DCSupplemental.

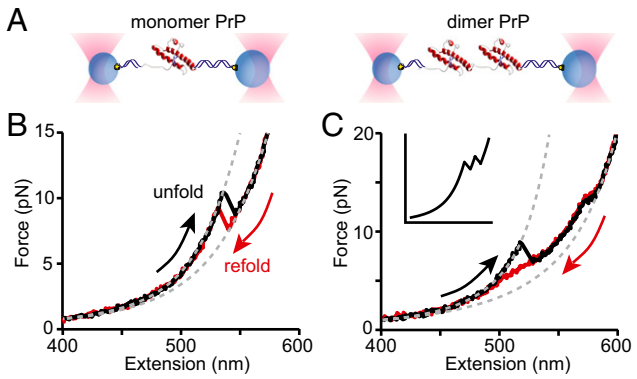

Fig. 1. FECs of PrP dimers reveal stable misfolded states. (*A*) Individual PrP molecules (*Left*, monomers; *Right*, dimers) attached to DNA handles were bound to beads held in optical traps. (*B*) Unfolding (black) and refolding (red) FECs of PrP monomers showing apparently two-state folding are well fit by WLC models (dashed lines). (*C*) Unfolding (black) and refolding (red) FECs of PrP dimers show the formation of stable nonnative structures, in contrast to the sequential unfolding of identical domains expected for independently folded native domains (cartoon, *Inset*).

Here we use SMFS to reconstruct the energy landscape for misfolding of the prion protein PrP and thereby recover D for misfolding. PrP is particularly interesting as a model for investigating protein misfolding, because even though PrP folds rapidly into its native structure (PrP^C) under normal conditions (31), it has a stable misfolded form, PrP^{Sc}, which can convert PrP^C to form more PrP^{Sc}, thereby acting as an infectious agent to transmit prion diseases (32). The structure of PrP^{Sc} remains unknown, as does the mechanism for conversion of PrP^C, although a variety of structural models (33) and mechanisms (32, 34) have been proposed. Previous single-molecule studies of PrP misfolding (35) have characterized properties such as the kinetics of oligomerization (30) and the dependence of aggregation pathways on metal ions (36), suggesting that the conversion of PrP features several phases starting with dimerization, but detailed pathways were not resolved. SMFS measurements of isolated PrP monomers found that they frequently sampled various misfolded conformations, but they were not thermodynamically stable, consistent with the view that misfolded PrP is stable only within aggregates (27).

Because the conversion of PrP may start with dimerization (30, 37), here we have focused on dimers as the smallest form of aggregate. Using optical tweezers to apply tension and thereby unfold and refold single PrP dimers, we found that dimers readily misfold into stable aggregates. A single misfolding pathway was observed and characterized in detail, revealing several exceptional features that set PrP apart from other proteins studied to date. Reconstruction of the energy landscape for dimer misfolding, along with the previously measured landscape for native folding (15), was then used to make the first comparison of D for native folding versus misfolding in the same protein, showing that diffusion is much slower during misfolding than during native folding.

Results

To study PrP misfolding, two hamster PrP molecules were covalently connected end to end, forming a tandem dimer (Fig. S1). Such tandem oligomers have been used previously to study misfolding and aggregation in a variety of proteins (38–40), including PrP (41). Tandem dimers were attached to DNA handles connected to beads held in dual-beam optical tweezers (27), as illustrated (Fig. 1*A*), and the force was ramped up/down to unfold/refold the molecules repeatedly while measuring their extension, thereby generating force-extension curves (FECs). The folding of two PrP molecules in close contact as tandem dimers was then compared with the folding of isolated monomers.

For isolated monomers, as described previously (27), the force increased monotonically as the DNA handles were stretched until the protein unfolded in a single step around 10 pN (Fig. 1*B*, black), creating a characteristic "rip" owing to the abrupt extension increase and concomitant force drop as the unfolded protein stretched out under tension. Refolding FECs retraced the same trajectory (Fig. 1*C*, red). The change in contour length during the transitions, ΔL_c, found by fitting 4,362 FECs to an extensible worm-like chain (WLC) model using Eq. **S1** agreed exactly with the result expected for natively structured PrP (42): 34.3 ± 0.4 nm.

For the dimer, two consecutive rips matching those for monomeric PrP would be expected (Fig. 1*C*, *Inset*) if each monomeric domain independently formed PrP^C, similar to the behavior typically observed in FECs of native folding in other tandem-repeat proteins (43–48). The actual behavior, however, was strikingly different, indicating that neither domain was natively folded. Unfolding FECs (Fig. 1*C*, black) often displayed one large rip at a force lower than native unfolding (~8 pN), followed by a shoulder-like region and then a distinctly smaller rip at a force higher than native unfolding (~13 pN). Refolding FECs retraced the small rip

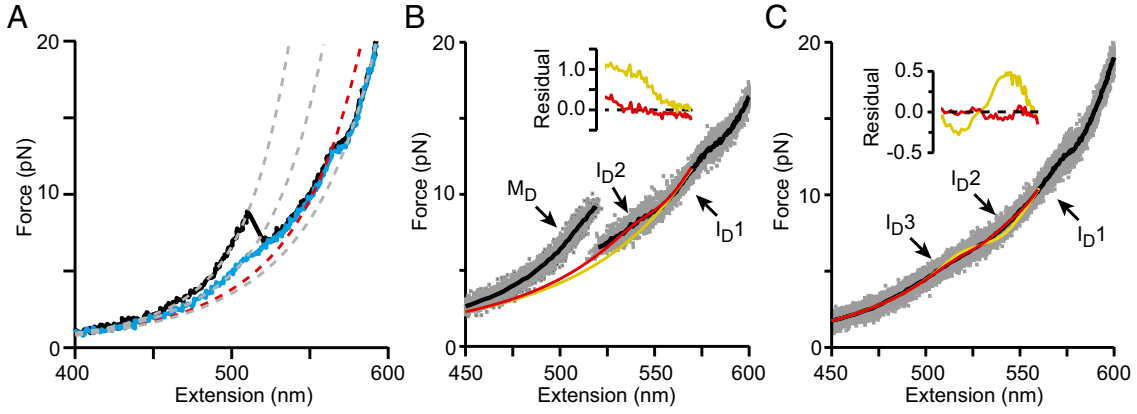

Fig. 2. Intermediates on the misfolding pathway of PrP dimers. (*A*) WLC fits (dashed lines) to representative type 1 (black) and 2 (blue) FECs reveal contour length changes (ΔL_c) in the dimer. The total ΔL_c (gray lines) is 56 nm for type 2 and 81 nm for type 1, compared with 34 nm for a single PrP^C domain. For both FEC types, an intermediate, I_D1 (red), unfolds at ~13 pN; a "shoulder" with non-WLC behavior at 5–10 pN indicates additional intermediates. (*B*) The shoulder feature in type 1 FECs was best fit assuming one additional transition (red) corresponding to I_D2–I_D1 transitions in type 2 FECs, rather than none (yellow), as shown by the residuals (*Inset*). (*C*) An average (black) of type 2 FECs (gray) was best fit in the shoulder region by a model assuming two additional transitions in sequence (red) rather than only one (yellow), as shown by the fit residuals (*Inset*). Unfolding occurred sequentially via three intermediates: I_D3, I_D2, and I_D1.

at high force, but not the large rip at lower force, displaying instead a broader shoulder region at 5–10 pN (Fig. 1*C*, red). Upon repeated unfolding–refolding cycles (Fig. S2), two classes of unfolding behavior were observed, denoted type 1 (Fig. 2*A*, black) and type 2 (Fig. 2*A*, blue). Type 2 unfolding FECs did not contain the large rip at low force, matching instead the shape of the refolding FECs. None of the curves showed behavior characteristic of natively folded PrP. The total ΔL_c for type 2 unfolding was 56 ± 3 nm (Fig. 2*A*, blue), corresponding to ∼170 aa in the misfolded structure, as opposed to 104 for PrP^C. In contrast, the total ΔL_c for type 1 unfolding was 81 ± 1 nm (Fig. 2*A*, black), corresponding to ∼240 aa, indicating that many of the residues unstructured in PrP^C were incorporated into the aggregated structure.

Such FECs contain all of the information required to reconstruct the misfolding energy landscape for the dimer. We first determined the sequence of states along the misfolding pathway. Multiple rips in the dimer FECs revealed several metastable intermediates, in contrast to two-state folding for native PrP (27). All unfolding and refolding FECs showed a discrete rip near 13 pN with ΔL_c = 15 ± 1 nm (Fig. 2*A* and Fig. S3); this state was denoted I_D1 (first dimer intermediate). FECs also contained a shoulder-like deviation from WLC behavior at 5–10 pN, arising from transitions that were fast compared with the rate at which force and extension were measured (14). Modeling the average curve expected in the shoulder region with Eq. **S2**, we found that type 1 unfolding curves were well fit assuming one additional intermediate between I_D1 and the fully misfolded state, M_D, which we denoted I_D2 (Fig. 2*B*). Type 2 unfolding curves required two sequential intermediates to obtain good fits (Fig. 2*C*); one had the same properties as I_D2, and the other was denoted I_D3 (Table 1). Type 1 unfolding thus followed the sequence of states $M_D \rightarrow I_D2 \rightarrow I_D1 \rightarrow U$ (unfolded state), whereas the sequence for type 2 unfolding was $I_D3 \rightarrow I_D2 \rightarrow I_D1 \rightarrow U$.

Refolding FECs retraced the type 2 unfolding curves and almost always ended in I_D3, without any observable transition into M_D (Fig. S4*A*). Very rarely, however, complete sequential refolding from U to M_D passing through each of the three intermediates was observed (Fig. S4*B*), indicating that all five states are actually on a single folding pathway. The fact that M_D was almost never observed directly during refolding suggests that it must form slowly at low force. Supporting this view, the fraction of curves exhibiting type 1 behavior could be increased by increasing the waiting time at low force between successive pulls (Fig. 3*A*). All FECs thus represent the same underlying pathway consisting of five sequential states: $M_D \leftrightarrow I_D3 \leftrightarrow I_D2 \leftrightarrow I_D1 \leftrightarrow U$ (Fig. 4*A*). Type 1 FECs do not show evidence for I_D3 because it has a lower unfolding force than M_D and hence the two states unfold concurrently. Notably, the final step in misfolding (formation of M_D) is much slower than native folding, with a rate of 0.5 s^{-1} compared with ∼10^4 s^{-1} for native PrP (15).

After elucidating the steps in the misfolding pathway, the energy landscape underlying the observed behavior was reconstructed from the unfolding forces and kinetics. For U, I_D1, I_D2, and I_D3, the free-energy differences between the states were found from the product of the unfolding forces and extension changes in the quasi-equilibrium transitions, whereas ΔG between M_D and I_D3 was found from the ratio of the state occupancies at long delay times. As a consistency check, we also found the total free energy change for complete unfolding by integrating the FECs to obtain the distribution of nonequilibrium work done on the molecule and then applying the Jarzysnki equality (49) to determine the free energy, as described previously (50). The result, ΔG_{total} = 23 ± 3 kcal/mol, agreed within error with the sum of the free energy changes for the individual transitions, 24 ± 2 kcal/mol. The locations and heights of the barriers between each state were found from the force-dependent unfolding rates (Fig. 3*B*), using the kinetic theory of Dudko et al. (51) (Eq. **S3**). Because discrete unfolding events could not be observed for the rapid transition between I_D2 and I_D1, the properties of the barrier between these states were not quantified. In the case of I_D1, the activation barrier to unfolding was the same within error (1 kcal/mol) as the equilibrium free energy of unfolding (Table 1), implying that there is a minimal barrier to refolding. Such a small barrier for refolding of I_D1 was confirmed by analyzing the refolding lifetimes (52) for the transition from U to I_D1 (Fig. S4*C*), which revealed a barrier of only about 1 kcal/mol.

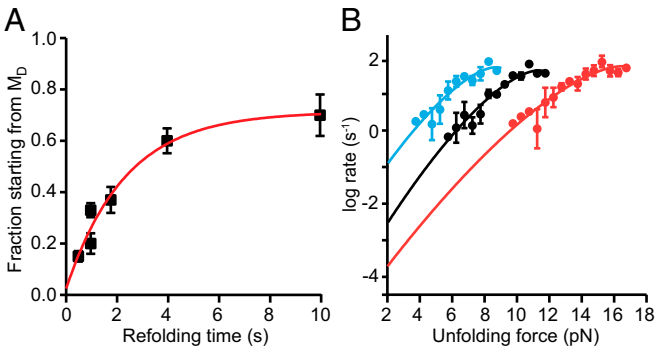

Fig. 3. Unfolding and refolding kinetics. (*A*) The fraction of type 1 FECs rose with the waiting time between successive pulls. Red line: single-exponential fit for the I_D3–M_D transition (0.5 ± 0.2 s^{-1}). (*B*) Force-dependent unfolding rates for M_D (black), I_D3 (blue), and I_D1 (red) fit to Eq. **S2** yield parameters describing the misfolding energy landscape.

All results from the analysis of the free energy differences and barrier properties (Table 1) were then combined piecewise for the five sequential states observed to reconstruct the energy landscape profile for the dimer misfolding (Fig. 4*B*). We note that, from this picture, once M_D has formed, the barrier to return to the native structure would be very high, ∼25 kcal/mol, because PrP^C could be formed only by passing through the unfolded state.

Finally, the diffusion coefficient implied by the barrier-crossing kinetics and landscape profile was determined for each of the three barriers reconstructed in the landscape, namely the transitions $M_D \leftrightarrow I_D3$, $I_D3 \leftrightarrow I_D2$, and $I_D1 \leftrightarrow U$, by refitting the force-dependent rates to the theory of Dudko et al. (51) reexpressed with D as an explicit fitting parameter (Eq. **S4**). Similar values were found for all three barriers: $D = 1 \times 10^{3 \pm 0.6}$ nm^2/s for unfolding M_D, $1 \times 10^{3 \pm 0.3}$ nm^2/s for unfolding I_D3, and $0.8 \times 10^{3 \pm 0.3}$ nm^2/s for unfolding I_D1. Because the value of D should be the same for both folding and unfolding, we also calculated D for refolding of I_D1; the result was $D = 3 \times 10^{3 \pm 0.4}$ nm^2/s, consistent within error with the unfolding result, for an average value for I_D1 of $1 \times 10^{3 \pm 0.3}$ nm^2/s. In all cases, errors were found by bootstrapping analysis (*SI Methods*). We note that D is exponentially sensitive to the barrier height in Kramers' theory analyses (17). Agreement between the values obtained for the unfolding and refolding of I_D1 is thus a strong test of self-consistency for the analysis, because the barrier heights differ by an order of magnitude between refolding and unfolding.

Table 1. Structural, kinetic, and energetic parameters of the misfolded dimer and intermediate states

Parameter	M_D	I_D3	I_D2	I_D1
ΔL_c to U from WLC fits, nm	81 ± 1	56 ± 3	—	15 ± 1
ΔL_c to next state from equilibrium fits, nm	—	23 ± 1	17 ± 2	14.4 ± 0.4
$F_{1/2}$ from equilibrium fits, pN	—	6.5 ± 0.4	8.5 ± 0.4	13.1 ± 0.5
ΔG to next state, kcal/mol	0.5 ± 0.1	6 ± 1	7 ± 1	11 ± 1
$\log(k_0)$, s^{-1}	−5 ± 1	−3.4 ± 0.6	—	−5.1 ± 0.6
$\Delta x^{\ddagger}$, nm	8 ± 2	7.8 ± 0.7	—	5.7 ± 0.7
$\Delta G^{\ddagger}$, kcal/mol	10 ± 1	8.0 ± 0.8	—	10.5 ± 0.8
$\log(D)$, nm^2/s	3.1 ± 0.6	3.1 ± 0.3	—	2.9 ± 0.3

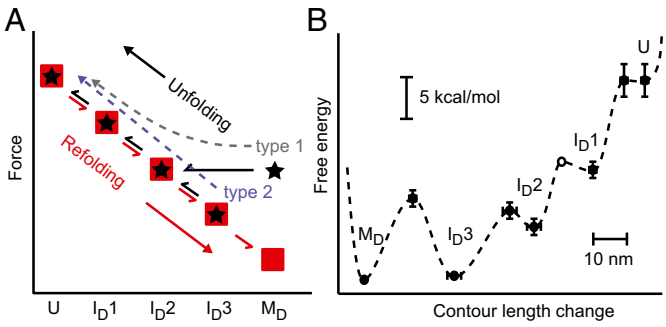

Fig. 4. Pathway and energy landscape for PrP dimer misfolding. (*A*) The folding pathway for the dimer (red) leads from U to M_D sequentially through each intermediate as the force is lowered. The unfolding pathway leads from M_D (type 1) or I_D3 (type 2) sequentially through each intermediate to U, skipping I_D3 in type 1 unfolding because of its low unfolding force. (*B*) PrP dimer misfolding energy landscape at zero force, reconstructed from FECs. Energy and contour length changes are plotted with respect to M_D (error bars: SEM).

Discussion

A central result of this analysis is that the diffusion coefficients found for misfolding transitions are significantly lower than the values found previously for unfolded proteins and peptides, by four to five orders of magnitude (5–10). More importantly, diffusion during misfolding of PrP is also significantly slower than diffusion during native folding. We previously reconstructed the landscape for native folding of PrP from SMFS measurements and used it to derive D by an analysis similar to that described above (15). For native folding, we found $D = 1 \times 10^{6\,\pm\,0.4}$ nm^2/s, indicating that diffusion during misfolding is about 1,000-fold slower than in native folding of the same protein.

Changes in D are often interpreted as arising from changes in the friction experienced by the protein chain, because $D = k_BT/\gamma$, where γ is the friction coefficient; γ may consist of friction from the viscous solvent or "internal" friction within the protein chain (53). Because both native folding and misfolding of PrP were measured under identical solvent conditions, the change in D most likely arises from differences in internal friction. Such friction is often modeled as additional roughness in the energy landscape: assuming a random roughness distribution along the 1D landscape profile, D is reduced by a factor of $\exp[-(\varepsilon/k_BT)^2]$, where ε is the rms roughness (54, 55). The observed 1,000-fold reduction in D for misfolding compared with native folding would in this picture reflect an additional 3 k_BT of roughness along the misfolding pathway.

Additional roughness like this indicates the presence of localized traps and barriers, presumably arising from a tendency to form many nonproductive or locally frustrated interactions while the protein is misfolding, interactions which, in contrast, are normally avoided during native folding. This picture agrees well with the notion that landscapes for native folding are expected to be smooth and minimally frustrated, owing to evolutionary selection for rapid, reliable folding into native structures, whereas the landscapes for proteins that are not subject to such evolutionary pressure are expected to exhibit more frustration, whether locally (resulting in higher roughness) or globally (resulting in a "flat" landscape that does not funnel the protein to a native, minimum-energy state) (56). Random-sequence polypeptides and artificially designed proteins have indeed been found both by experiment (57) and simulation (58) to exhibit a greater prevalence of mutually exclusive competing interactions frustrating the folding, compared with naturally evolved natively folded proteins. It has generally been presumed that nonnative structure formation also involves unusually rough landscapes (21), owing similarly to the lack of selective pressure to reduce frustration, but until now this picture has not been verified experimentally by quantifying the difference in roughness between misfolding and native folding for the same protein.

We note that our analysis is based implicitly on Kramers' widely used theory of diffusive barrier crossing, wherein the diffusion coefficient is approximated as constant (2, 59). In fact, owing to the effects of projecting the full multidimensional energy landscape onto a one-dimensional reaction coordinate, in theory D is expected to vary with position (59–61). Although the position dependence of D is challenging to measure experimentally, current evidence suggests that the variation in D is less than an order of magnitude (6, 62, 63), far too small to account for the large difference between native and misfolded PrP. To verify that the constant-D approximation was indeed reasonable, we examined the average transit time, τ_{tp}, required to cross the barrier during the misfolding: τ_{tp} is a sensitive probe of D that is, in contrast, insensitive to the barrier height, and moreover can be measured directly without assumptions about the form of D (11, 17).

The $I_D1 \leftrightarrow U$ transition was measured in equilibrium using a passive force clamp (64) to keep the force near $F_{1/2}$, and segments of the trajectory containing the transitions between I_D1 and U were extracted similarly to previous work (27) on transitions during native folding of PrP (Fig. 5*A*). The transition time was measured directly from the trajectory segments, as the time required to traverse the middle half of the distance between I_D1 and U (Fig. 5*B*). Whereas τ_{tp} was found from energy landscape analysis of native folding to be 2 μs, faster than the 50-μs time resolution of the instrument (13, 15), the $I_D1 \leftrightarrow U$ transition time was much slower, with many transitions occurring on the millisecond timescale—slow enough that individual transition paths themselves could be clearly resolved (Fig. 5 *B* and *C*). Averaging over 1,500 transitions, we found $\tau_{tp} = 0.5 \pm 0.1$ ms for unfolding and 0.5 ± 0.1 ms for refolding, roughly 300 times longer than for native folding and thus reflecting an orders-of-magnitude increase in D. For comparison, the value for τ_{tp} can be predicted from the result for D using Eq. **S5**, assuming a harmonic barrier with constant D. The result, $\tau_{tp} = 1 \times 10^{0\,\pm\,0.3}$ ms, is fully consistent with the directly measured value, confirming the robustness of the landscape analysis above.

Looking beyond the diffusion coefficient, analysis of the misfolding pathway revealed several exceptional features that contrast PrP with other proteins studied to date. Surprisingly, PrP dimers misfolded remarkably easily, invariably following a single pathway leading to the same state. Such homogeneous misfolding contrasts sharply with the heterogeneity seen in SMFS studies of

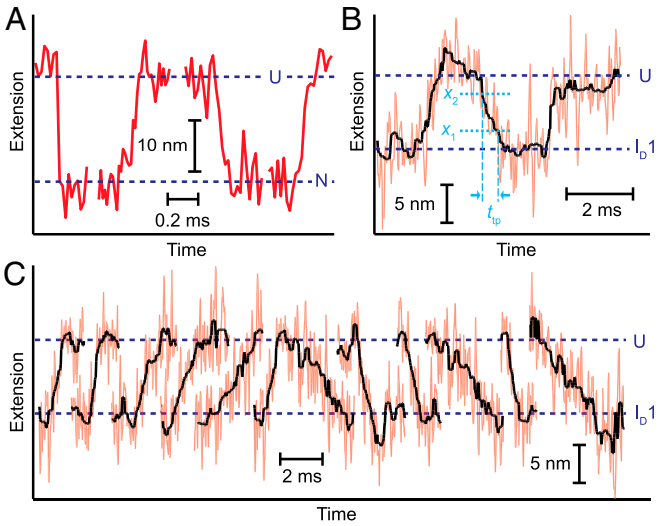

Fig. 5. Transition path time measurements. (*A*) Native folding transitions measured from constant-force trajectories occur faster than the resolution limit of the tweezers, 50 μs. (*B*) The transition path time for misfolding measured from constant-force trajectories for I_D1 folding is much slower. The transit time in each transition, t_{tp}, was measured as the time taken to cross the barrier region defined by the boundaries x_1 and x_2 (dotted lines). (*C*) Transitions between U and I_D1 were as slow as the millisecond timescale.

dimers of other aggregation-prone proteins, such as α-synuclein (39) and Aβ (65). The high rate of misfolding also differs starkly from most previous single-molecule studies of tandem-repeat proteins, where misfolding—if it was observed at all—occurred at much lower levels, for example, 2–5% of the time for titin I27 domain repeats (66, 67), 4% for tenascin FN III repeats (67), 3–8% for spectrin repeats (68), and 15–30% for α-synuclein repeats (39). Another key difference from these other proteins, as well as from monomeric PrP (27), concerns the stability of the misfolded states: Whereas in previous studies the misfolded states were only metastable, eventually converting back to the native structure [whether rapidly (27) or slowly (66, 67)], our results show the misfolded PrP dimer to be thermodynamically stable (24 ± 2 kcal/mol for M_D versus 11 ± 1 kcal/mol per native monomer). These features suggest that PrP may be particularly predisposed to conversion into specific misfolded structures through intermolecular interactions. Indeed, PrP dimer misfolding looks remarkably like the native folding of a protein that has evolved to have a well-funneled, minimally frustrated landscape (56), without the heterogeneous pathways expected for aggregation (21). The primary sign that nonnative interactions are involved is the strikingly slow diffusion coefficient.

We note that the stability of M_D cannot alone explain the exclusively misfolded behavior, because the small energy difference between M_D and PrP^C (~2 kcal/mol) should lead to an equilibrium PrP^C population of ~4% in the dimer. Hence, there must also be some kinetic selection for misfolding. This observation suggests a mechanism for the misfolding: The intermediate I_D1, which forms at a higher force than does PrP^C, prevents the formation of PrP^C in either domain, thereby promoting misfolding. Indeed, because I_D1 does not form in monomeric PrP (27), it must involve interactions between C-terminal residues in one domain of the dimer and N-terminal residues of the other (Fig. S5), which then form an interdomain nucleus for the misfolding. From the 15-nm contour length change upon unfolding, we estimate that I_D1 consists of ~50 aa. It thus almost certainly encompasses the region spanning the link between the two domains (i.e., the C-terminal residues of the first domain and the N-terminal residues of the second domain).

Finally, it is interesting to speculate as to the structure of the misfolded dimer. CD spectra revealed a substantial conversion from primarily helices in the monomer (Fig. S6, black) to primarily β-strands in the dimer (Fig. S6, red). Conversion to a soluble, β-rich form, induced by low pH and/or mildly denaturing conditions, has been studied previously as a potential intermediate step in PrP^{Sc} formation (69, 70). Here, however, low pH is not required: β-rich structures are seen both at pH 4 and neutral pH. At the ensemble level, the PrP dimer forms an oligomer that rapidly precipitates under conditions of pH and ionic strength like those used during the SMFS measurements, similar to previous reports (41). It is possible that the individual misfolded dimers undergo additional restructuring upon oligomerization; nevertheless, the single-molecule misfolded form is likely rich in β-strands, serving as the precursor to the bulk oligomers. The low dimer helical content is consistent with models of PrP aggregates (33) in which the helical C terminus of PrP^C is converted to β-strands—in contrast to those positing the retention of significant C-terminal helical content—as well as with single-molecule fluorescence results finding β-rich dimers as the first step in PrP aggregation (30). Suggestively, PrP dimers were proposed to play a role in the conversion of PrP^C to PrP^{Sc} (37) and synthetic dimers have been shown to be neurotoxic both in culture and in mouse models (41). Synthetic dimers have also been used effectively as immunogens to elicit antiprion antibodies to reduce PrP^{Sc} formation (71). However, the relevance of the species observed at the single-molecule level to disease remains to be established in future work.

Despite the complexity of protein misfolding and aggregation, these results show that the energy landscape can be resolved in the single-molecule limit and used to probe crucial properties such as the diffusion coefficient setting the timescale for microscopic motions. This work opens the possibility of investigating the fundamental biophysical factors driving structural outcomes in misfolding and aggregation.

Methods

Sample Preparation. Dimers of Syrian hamster PrP(91–231) were made either by linking PrP monomers via disulfide bonds between cysteine residues engineered at the termini or by recombinant expression of a single tandem-repeat gene. See *SI Methods* for complete details.

FEC Measurements and Analysis. FECs were measured with dual-trap optical tweezers as described (15, 27). ΔL_c values were found by fitting the different branches of the FECs to extensible WLC models (Eq. **S1**) for the DNA handles and unfolded protein (27). The shoulder feature at low force was fit using a model of the average extension and force expected in the case of rapid, equilibrated transitions assuming two-state behavior (Eq. **S2**). Unfolding-force histograms were converted into force-dependent rates and fit using Eq. **S3**, yielding the unfolding rate at zero force, k_0, the distance to the transition state from the folded state, $\Delta x^{\ddagger}$, and the energy barrier height, $\Delta G^{\ddagger}$ (51). See *SI Methods* for complete details.

Energy Landscape Parameters. ΔG between U, I_D1, I_D2, and I_D3 was found from the unfolding forces and extension changes during the quasi-equilibrium transitions: $\Delta G = \Delta x(F_{1/2})\cdot F_{1/2} - \Delta G_{stretch}$, where $\Delta G_{stretch}$ is the energy for stretching the unfolded protein to $F_{1/2}$, found by integrating the WLC model for the protein alone. ΔG between M_D and I_D3 was found from the ratio of the state occupancies at long delay times: $\Delta G = k_BT\ln(M_D/I_D3)$. ΔG_{total} for complete unfolding was also found from the Jarzynski equality: $\Delta G_{total} = -k_BT\ln\langle\exp(-W/k_BT)\rangle - \Delta G_{stretch}$, where W is the irreversible work done to unfold the entire protein found by integrating the FECs, $\Delta G_{stretch}$ is the reversible stretching energy of the handles and unfolded protein, and the finite sampling bias was corrected (72). Barrier heights and positions were found from the kinetic fits described above. The combination of methods used to reconstruct the energy landscape is illustrated in Fig. S7.

Diffusion Coefficient. D was found for each barrier by fitting the force-dependent rates to Eq. **S4**. See *SI Methods* for complete details.

ACKNOWLEDGMENTS. This work was supported by funds from PrioNet Canada, Alberta Prion Research Institute, Alberta Innovates (AI) Technology Futures, AI Health Solutions, Natural Sciences and Engineering Research Council, and the National Institute for Nanotechnology.

1. Dill KA, MacCallum JL (2012) The protein-folding problem, 50 years on. *Science* 338(6110):1042–1046.
2. Hanggi P, Talkner P, Borkovec M (1990) Reaction-rate theory - 50 years after Kramers. *Rev Mod Phys* 62(2):251–341.
3. Hagen SJ (2010) Solvent viscosity and friction in protein folding dynamics. *Curr Protein Pept Sci* 11(5):385–395.
4. Kubelka J, Hofrichter J, Eaton WA (2004) The protein folding 'speed limit'. *Curr Opin Struct Biol* 14(1):76–88.
5. Ahmad B, Chen Y, Lapidus LJ (2012) Aggregation of α-synuclein is kinetically controlled by intramolecular diffusion. *Proc Natl Acad Sci USA* 109(7):2336–2341.
6. Borgia A, et al. (2012) Localizing internal friction along the reaction coordinate of protein folding by combining ensemble and single-molecule fluorescence spectroscopy. *Nat Commun* 3:1195.
7. Hagen SJ, Hofrichter J, Szabo A, Eaton WA (1996) Diffusion-limited contact formation in unfolded cytochrome c: Estimating the maximum rate of protein folding. *Proc Natl Acad Sci USA* 93(21):11615–11617.
8. Möglich A, Joder K, Kiefhaber T (2006) End-to-end distance distributions and intrachain diffusion constants in unfolded polypeptide chains indicate intramolecular hydrogen bond formation. *Proc Natl Acad Sci USA* 103(33):12394–12399.
9. Soranno A, et al. (2012) Quantifying internal friction in unfolded and intrinsically disordered proteins with single-molecule spectroscopy. *Proc Natl Acad Sci USA* 109(44):17800–17806.
10. Waldauer SA, Bakajin O, Lapidus LJ (2010) Extremely slow intramolecular diffusion in unfolded protein L. *Proc Natl Acad Sci USA* 107(31):13713–13717.
11. Chung HS, Eaton WA (2013) Single-molecule fluorescence probes dynamics of barrier crossing. *Nature* 502(7473):685–688.
12. Lannon H, Haghpanah JS, Montclare JK, Vanden-Eijnden E, Brujic J (2013) Force-clamp experiments reveal the free-energy profile and diffusion coefficient of the collapse of protein molecules. *Phys Rev Lett* 110(12):128301.
13. Neupane K, et al. (2012) Transition path times for nucleic acid folding determined from energy-landscape analysis of single-molecule trajectories. *Phys Rev Lett* 109(6):068102.

14. Solanki A, Neupane K, Woodside MT (2014) Single-molecule force spectroscopy of rapidly fluctuating, marginally stable structures in the intrinsically disordered protein α-synuclein. *Phys Rev Lett* 112(15):158103.
15. Yu H, et al. (2012) Energy landscape analysis of native folding of the prion protein yields the diffusion constant, transition path time, and rates. *Proc Natl Acad Sci USA* 109(36):14452–14457.
16. Woodside MT, Block SM (2014) Reconstructing folding energy landscapes by single-molecule force spectroscopy. *Annu Rev Biophys* 43:19–39.
17. Woodside MT, Lambert J, Beach KSD (2014) Determining intrachain diffusion coefficients for biopolymer dynamics from single-molecule force spectroscopy measurements. *Biophys J* 107(7):1647–1653.
18. Chiti F, Dobson CM (2006) Protein misfolding, functional amyloid, and human disease. *Annu Rev Biochem* 75:333–366.
19. Johnson SM, et al. (2005) Native state kinetic stabilization as a strategy to ameliorate protein misfolding diseases: A focus on the transthyretin amyloidoses. *Acc Chem Res* 38(12):911–921.
20. Zheng W, Schafer NP, Wolynes PG (2013) Free energy landscapes for initiation and branching of protein aggregation. *Proc Natl Acad Sci USA* 110(51):20515–20520.
21. Jahn TR, Radford SE (2008) Folding versus aggregation: Polypeptide conformations on competing pathways. *Arch Biochem Biophys* 469(1):100–117.
22. Eichner T, Kalverda AP, Thompson GS, Homans SW, Radford SE (2011) Conformational conversion during amyloid formation at atomic resolution. *Mol Cell* 41(2):161–172.
23. Neudecker P, et al. (2012) Structure of an intermediate state in protein folding and aggregation. *Science* 336(6079):362–366.
24. Laganowsky A, et al. (2012) Atomic view of a toxic amyloid small oligomer. *Science* 335(6073):1228–1231.
25. Hoffmann A, Neupane K, Woodside MT (2013) Single-molecule assays for investigating protein misfolding and aggregation. *Phys Chem Chem Phys* 15(21):7934–7948.
26. Stigler J, Ziegler F, Gieseke A, Gebhardt JC, Rief M (2011) The complex folding network of single calmodulin molecules. *Science* 334(6055):512–516.
27. Yu H, et al. (2012) Direct observation of multiple misfolding pathways in a single prion protein molecule. *Proc Natl Acad Sci USA* 109(14):5283–5288.
28. Heidarsson PO, et al. (2014) Direct single-molecule observation of calcium-dependent misfolding in human neuronal calcium sensor-1. *Proc Natl Acad Sci USA* 111(36): 13069–13074.
29. Cremades N, et al. (2012) Direct observation of the interconversion of normal and toxic forms of α-synuclein. *Cell* 149(5):1048–1059.
30. Post K, et al. (1998) Rapid acquisition of beta-sheet structure in the prion protein prior to multimer formation. *Biol Chem* 379(11):1307–1317.
31. Wildegger G, Liemann S, Glockshuber R (1999) Extremely rapid folding of the C-terminal domain of the prion protein without kinetic intermediates. *Nat Struct Biol* 6(6): 550–553.
32. Colby DW, Prusiner SB (2011) Prions. *Cold Spring Harb Perspect Biol* 3(1):a006833.
33. Diaz-Espinoza R, Soto C (2012) High-resolution structure of infectious prion protein: the final frontier. *Nat Struct Mol Biol* 19(4):370–377.
34. Cobb NJ, Sönnichsen FD, McHaourab H, Surewicz WK (2007) Molecular architecture of human prion protein amyloid: a parallel, in-register beta-structure. *Proc Natl Acad Sci USA* 104(48):18946–18951.
35. Yu H, Dee DR, Woodside MT (2013) Single-molecule approaches to prion protein misfolding. *Prion* 7(2):140–146.
36. Levin J, Bertsch U, Kretzschmar H, Giese A (2005) Single particle analysis of manganese-induced prion protein aggregates. *Biochem Biophys Res Commun* 329(4): 1200–1207.
37. Tompa P, Tusnády GE, Friedrich P, Simon I (2002) The role of dimerization in prion replication. *Biophys J* 82(4):1711–1718.
38. Bader R, Bamford R, Zurdo J, Luisi BF, Dobson CM (2006) Probing the mechanism of amyloidogenesis through a tandem repeat of the PI3-SH3 domain suggests a generic model for protein aggregation and fibril formation. *J Mol Biol* 356(1):189–208.
39. Neupane K, Solanki A, Sosova I, Belov M, Woodside MT (2014) Diverse metastable structures formed by small oligomers of α-synuclein probed by force spectroscopy. *PLoS ONE* 9(1):e86495.
40. Speretta E, et al. (2012) Expression in drosophila of tandem amyloid β peptides provides insights into links between aggregation and neurotoxicity. *J Biol Chem* 287(24): 20748–20754.
41. Simoneau S, et al. (2007) In vitro and in vivo neurotoxicity of prion protein oligomers. *PLoS Pathog* 3(8):e125.
42. James TL, et al. (1997) Solution structure of a 142-residue recombinant prion protein corresponding to the infectious fragment of the scrapie isoform. *Proc Natl Acad Sci USA* 94(19):10086–10091.
43. Cao Y, Li H (2007) Polyprotein of GB1 is an ideal artificial elastomeric protein. *Nat Mater* 6(2):109–114.
44. Carrion-Vazquez M, et al. (2003) The mechanical stability of ubiquitin is linkage dependent. *Nat Struct Biol* 10(9):738–743.
45. Dietz H, Berkemeier F, Bertz M, Rief M (2006) Anisotropic deformation response of single protein molecules. *Proc Natl Acad Sci USA* 103(34):12724–12728.
46. Jollymore A, Lethias C, Peng Q, Cao Y, Li H (2009) Nanomechanical properties of tenascin-X revealed by single-molecule force spectroscopy. *J Mol Biol* 385(4): 1277–1286.
47. Rief M, Pascual J, Saraste M, Gaub HE (1999) Single molecule force spectroscopy of spectrin repeats: Low unfolding forces in helix bundles. *J Mol Biol* 286(2):553–561.
48. Rief M, Gautel M, Oesterhelt F, Fernandez JM, Gaub HE (1997) Reversible unfolding of individual titin immunoglobulin domains by AFM. *Science* 276(5315):1109–1112.
49. Jarzynski C (1997) Nonequilibrium equality for free energy differences. *Phys Rev Lett* 78:2690–2693.
50. Greenleaf WJ, Frieda KL, Foster DA, Woodside MT, Block SM (2008) Direct observation of hierarchical folding in single riboswitch aptamers. *Science* 319(5863):630–633.
51. Dudko OK, Hummer G, Szabo A (2008) Theory, analysis, and interpretation of single-molecule force spectroscopy experiments. *Proc Natl Acad Sci USA* 105(41):15755–15760.
52. Pierse CA, Dudko OK (2013) Kinetics and energetics of biomolecular folding and binding. *Biophys J* 105(9):L19–L22.
53. Ansari A, Jones CM, Henry ER, Hofrichter J, Eaton WA (1992) The role of solvent viscosity in the dynamics of protein conformational changes. *Science* 256(5065): 1796–1798.
54. Bryngelson JD, Wolynes PG (1989) Intermediates and barrier crossing in a random energy-model (with applications to protein folding). *J Phys Chem* 93(19):6902–6915.
55. Zwanzig R (1988) Diffusion in a rough potential. *Proc Natl Acad Sci USA* 85(7): 2029–2030.
56. Onuchic JN, Wolynes PG (2004) Theory of protein folding. *Curr Opin Struct Biol* 14(1): 70–75.
57. Scalley-Kim M, Baker D (2004) Characterization of the folding energy landscapes of computer generated proteins suggests high folding free energy barriers and cooperativity may be consequences of natural selection. *J Mol Biol* 338(3):573–583.
58. Truong HH, Kim BL, Schafer NP, Wolynes PG (2013) Funneling and frustration in the energy landscapes of some designed and simplified proteins. *J Chem Phys* 139(12): 121908.
59. Best RB, Hummer G (2010) Coordinate-dependent diffusion in protein folding. *Proc Natl Acad Sci USA* 107(3):1088–1093.
60. Chahine J, Oliveira RJ, Leite VB, Wang J (2007) Configuration-dependent diffusion can shift the kinetic transition state and barrier height of protein folding. *Proc Natl Acad Sci USA* 104(37):14646–14651.
61. Oliveira RJ, Whitford PC, Chahine J, Leite VB, Wang J (2010) Coordinate and time-dependent diffusion dynamics in protein folding. *Methods* 52(1):91–98.
62. Best RB, Hummer G (2006) Diffusive model of protein folding dynamics with Kramers turnover in rate. *Phys Rev Lett* 96(22):228104.
63. Cellmer T, Henry ER, Hofrichter J, Eaton WA (2008) Measuring internal friction of an ultrafast-folding protein. *Proc Natl Acad Sci USA* 105(47):18320–18325.
64. Greenleaf WJ, Woodside MT, Abbondanzieri EA, Block SM (2005) Passive all-optical force clamp for high-resolution laser trapping. *Phys Rev Lett* 95(20):208102.
65. Kim BH, et al. (2011) Single-molecule atomic force microscopy force spectroscopy study of Aβ-40 interactions. *Biochemistry* 50(23):5154–5162.
66. Borgia MB, et al. (2011) Single-molecule fluorescence reveals sequence-specific misfolding in multidomain proteins. *Nature* 474(7353):662–665.
67. Oberhauser AF, Marszalek PE, Carrion-Vazquez M, Fernandez JM (1999) Single protein misfolding events captured by atomic force microscopy. *Nat Struct Biol* 6(11): 1025–1028.
68. Randles LG, Rounsevell RW, Clarke J (2007) Spectrin domains lose cooperativity in forced unfolding. *Biophys J* 92(2):571–577.
69. Baskakov IV, Legname G, Baldwin MA, Prusiner SB, Cohen FE (2002) Pathway complexity of prion protein assembly into amyloid. *J Biol Chem* 277(24):21140–21148.
70. Bjorndahl TC, et al. (2011) Detailed biophysical characterization of the acid-induced PrP(c) to PrP(β) conversion process. *Biochemistry* 50(7):1162–1173.
71. Gilch S, et al. (2003) Polyclonal anti-PrP auto-antibodies induced with dimeric PrP interfere efficiently with PrPSc propagation in prion-infected cells. *J Biol Chem* 278(20):18524–18531.
72. Gore J, Ritort F, Bustamante C (2003) Bias and error in estimates of equilibrium free-energy differences from nonequilibrium measurements. *Proc Natl Acad Sci USA* 100(22):12564–12569.
73. Zheng P, Cao Y, Li H (2011) Facile method of constructing polyproteins for single-molecule force spectroscopy studies. *Langmuir* 27(10):5713–5718.
74. Shank EA, Cecconi C, Dill JW, Marqusee S, Bustamante C (2010) The folding cooperativity of a protein is controlled by its chain topology. *Nature* 465(7298):637–640.
75. Moffitt JR, Chemla YR, Smith SB, Bustamante C (2008) Recent advances in optical tweezers. *Annu Rev Biochem* 77:205–228.
76. Žoldák G, Stigler J, Pelz B, Li H, Rief M (2013) Ultrafast folding kinetics and cooperativity of villin headpiece in single-molecule force spectroscopy. *Proc Natl Acad Sci USA* 110(45):18156–18161.
77. Dudko OK, Hummer G, Szabo A (2006) Intrinsic rates and activation free energies from single-molecule pulling experiments. *Phys Rev Lett* 96(10):108101.
78. Zhang Y, Dudko OK (2013) A transformation for the mechanical fingerprints of complex biomolecular interactions. *Proc Natl Acad Sci USA* 110(41):16432–16437.
79. Yang WY, Gruebele M (2003) Folding at the speed limit. *Nature* 423(6936):193–197.
80. Janovjak H, Knaus H, Muller DJ (2007) Transmembrane helices have rough energy surfaces. *J Am Chem Soc* 129(2):246–247.
81. Wensley BG, et al. (2010) Experimental evidence for a frustrated energy landscape in a three-helix-bundle protein family. *Nature* 463(7281):685–688.
82. Pfitzner E, et al. (2013) Rigid DNA beams for high-resolution single-molecule mechanics. *Angew Chem Int Ed Engl* 52(30):7766–7771.
83. Seol Y, Perkins T (2009) Sensitivity of DNA-hairpins dynamics to the mechanism of force feedback probed using a surface-coupled passive force clamp. *Biophys J* 96(3, Suppl 1):291a.
84. Chaudhury S, Makarov DE (2010) A harmonic transition state approximation for the duration of reactive events in complex molecular rearrangements. *J Chem Phys* 133(3):034118.
85. Chung HS, Louis JM, Eaton WA (2009) Experimental determination of upper bound for transition path times in protein folding from single-molecule photon-by-photon trajectories. *Proc Natl Acad Sci USA* 106(29):11837–11844.